

ESPRESSO reveals blueshifted neutral iron emission lines on the dayside of WASP-76 b [★]

A. R. Costa Silva^{1,2,3}, O. D. S. Demangeon^{1,2}, N. C. Santos^{1,2}, D. Ehrenreich^{3,4}, C. Lovis³, H. Chakraborty³, M. Lendl³, F. Pepe³, S. Cristiani⁵, R. Rebolo^{6,7,8}, M. R. Zapatero-Osorio⁹, V. Adibekyan^{1,2}, Y. Alibert¹⁰, R. Allart^{11,3**}, C. Allende Prieto^{6,7}, T. Azevedo Silva^{1,2}, F. Borsa¹², V. Bourrier³, E. Cristo^{1,2}, P. Di Marcantonio⁵, E. Esparza-Borges^{6,7}, P. Figueira^{3,1}, J. I. González Hernández^{6,7}, E. Herrero-Cisneros¹³, G. Lo Curto¹⁴, C. J. A. P. Martins^{1,15}, A. Mehner¹⁴, N. J. Nunes¹⁶, E. Palle^{6,7}, S. Pelletier³, J. V. Seidel¹⁴, A. M. Silva^{1,2}, S. G. Sousa¹, A. Sozzetti¹⁷, M. Steiner³, A. Suárez Mascareño^{6,7}, and S. Udry³

¹ Instituto de Astrofísica e Ciências do Espaço, Universidade do Porto, CAUP, Rua das Estrelas, 4150-762 Porto, Portugal

² Departamento de Física e Astronomia, Faculdade de Ciências, Universidade do Porto, Rua do Campo Alegre, 4169-007 Porto, Portugal

³ Observatoire Astronomique de l'Université de Genève, Chemin Pegasi 51, 1290 Versoix, Switzerland

⁴ Centre Vie dans l'Univers, Faculté des sciences, Université de Genève, Genève 4, Switzerland

⁵ INAF – Osservatorio Astronomico di Trieste, via G. B. Tiepolo 11, I-34143, Trieste, Italy

⁶ Instituto de Astrofísica de Canarias, c/ Vía Láctea s/n, 38205 La Laguna, Tenerife, Spain

⁷ Departamento de Astrofísica, Universidad de La Laguna, 38206 La Laguna, Tenerife, Spain

⁸ Consejo Superior de Investigaciones Científicas, Spain

⁹ Centro de Astrobiología, CSIC-INTA, Camino Bajo del Castillo s/n, E-28692 Villanueva de la Cañada, Madrid, Spain

¹⁰ Physics Institute, University of Bern, Sidlerstrasse 5, 3012 Bern, Switzerland

¹¹ Département de Physique, Institut Trottier de Recherche sur les Exoplanètes, Université de Montréal, Montréal, Québec, H3T 1J4, Canada

¹² INAF – Osservatorio Astronomico di Brera, Via E. Bianchi 46, 23807 Merate (LC), Italy

¹³ Centro de Astrobiología, CSIC-INTA, Crta. Ajalvir km 4, E-28850 Torrejón de Ardoz, Madrid, Spain

¹⁴ European Southern Observatory, Alonso de Córdova 3107, Vitacura, Región Metropolitana, Chile

¹⁵ Centro de Astrofísica da Universidade do Porto, Rua das Estrelas, 4150-762 Porto, Portugal

¹⁶ Instituto de Astrofísica e Ciências do Espaço, Faculdade de Ciências da Universidade de Lisboa, Campo Grande, PT1749-016 Lisboa, Portugal

¹⁷ INAF – Osservatorio Astrofisico di Torino, Via Osservatorio 20, 10025 Pino Torinese, Italy

Received 11 March 2024; accepted 9 July 2024

ABSTRACT

Context. Ultra hot Jupiters (gas giants with $T_{\text{eq}} > 2000$ K) are intriguing exoplanets due to the extreme physics and chemistry present in their atmospheres. Their torrid daysides can be characterised using ground-based high-resolution emission spectroscopy.

Aims. We search for signatures of neutral and singly ionised iron (Fe I and Fe II, respectively) in the dayside of the ultra hot Jupiter WASP-76 b, as these species were detected via transmission spectroscopy in this exoplanet. Furthermore, we aim to confirm the existence of a thermal inversion layer, which has been reported in previous studies, and attempt to constrain its properties.

Methods. We observed WASP-76 b on four epochs with ESPRESSO at the VLT, at orbital phases shortly before and after the secondary transit, when the dayside is in view. We present the first analysis of high-resolution optical emission spectra for this exoplanet. We compare the data to synthetic templates created with `petitRADTRANS`, using cross-correlation function techniques.

Results. We detect a blueshifted (-4.7 ± 0.3 km/s) Fe I emission signature on the dayside of WASP-76 b at 6.0σ . The signal is detected independently both before and after the eclipse, and it is blueshifted in both cases. The presence of iron emission features confirms the existence of a thermal inversion layer. Fe II was not detected, possibly because this species is located in the upper layers of the atmosphere, which are more optically thin. Thus the Fe II signature on the dayside of WASP-76 b is too weak to be detected with emission spectroscopy.

Conclusions. We propose that the blueshifted Fe I signature is created by material rising from the hot spot to the upper layers of the atmosphere, and discuss possible scenarios related to the position of the hotspot. This work unveils some of the dynamic processes ongoing on the dayside of the ultra hot Jupiter WASP-76 b through the analysis of the Fe I signature from its atmosphere, and complements previous knowledge obtained from transmission studies. It also highlights the ability of ESPRESSO to probe the dayside of this class of exoplanets.

Key words. Methods: observational – Techniques: spectroscopic – Planets and satellites: atmospheres – Planets and satellites: gaseous planets – Planets and satellites: individual: WASP-76 b

1. Introduction

In recent years, the field of exoplanet research has partially shifted its focus from the detection of other worlds to their detailed characterisation. The study of exoplanet atmospheres provides extensive knowledge that helps us constrain the formation and evolution models of exoplanetary systems (e.g. Madhusudhan 2019), and it is also considered a crucial step in the search for extraterrestrial life (e.g. Schwietzman et al. 2018; Meadows et al. 2018).

Ultra hot Jupiters (UHJs) are an interesting class of exoplanets to further characterise, due to their extreme equilibrium temperatures ($T_{\text{eq}} > 2000$ K) and even hotter dayside temperatures. It has been predicted that thermal inversion layers exist on the dayside of these scorched planets (e.g. Lothringer et al. 2018; Lothringer & Barman 2019), that is a hotter layer of atmosphere on top of a colder layer, where chemical species produce emission features. Recent observational studies have confirmed this by probing the emission spectra of exoplanets during orbital phases close to the secondary transit (also known as eclipse or occultation), and detecting such features (e.g. Evans et al. 2017; Yan et al. 2020; Borsa et al. 2022; Changeat et al. 2022).

However, it is still unclear what species are absorbing the stellar irradiation at high altitudes and creating the inversion. For some time, titanium oxide (TiO) and vanadium oxide (VO) were assumed to be the opacity sources responsible for this feature (Hubeny et al. 2003; Fortney et al. 2008). Though more recently, Lothringer et al. (2018) have shown that neutral iron (Fe I) and other atomic metals are also capable of creating an inversion in the atmospheres of UHJs, without the need for TiO or VO. Fe I detections have been reported in multiple UHJs, both in the terminators and on the dayside, through transmission spectroscopy (e.g. Hoeijmakers et al. 2018; Ehrenreich et al. 2020; Bourrier et al. 2020; Borsa et al. 2021) and emission spectroscopy (e.g. Pino et al. 2020; Scandariato et al. 2023), respectively.

Detecting singly ionised iron (Fe II) is also of interest, as it could shed some light on the effect that magnetic fields have on the atmosphere of UHJs (e.g. Perna et al. 2010), and inform modelling works regarding the ionisation (and recombination) fraction of iron. Fe II has been detected in several hot giants via transmission studies (e.g. Hoeijmakers et al. 2019; Borsa et al. 2021; Prinoth et al. 2022; Bello-Arufe et al. 2022), however, it has only been detected once in emission observations of a UHJ. Borsa et al. (2021) reported Fe II in the post-eclipse observation of KELT-20 b/MASCARA-2 b, but follow-up studies have not been able to confirm the detection (Yan et al. 2022; Kasper et al. 2023; Petz et al. 2024). Further non-detections have been reported for KELT-9 b (Pino et al. 2020; Ridden-Harper et al. 2023), WASP-33 b (Cont et al. 2022), and WASP-121 b (Hoeijmakers et al. 2024).

The target of our study is WASP-76 b (West et al. 2016), an UHJ orbiting an F7-star ($V = 9.52$ mag) on a 1.81-day period, at a separation of 0.033 AU (the parameters of WASP-76 b and its host star are listed in Table 1). The equilibrium temperature of this exoplanet is $T_{\text{eq}} \sim 2228$ K (Ehrenreich et al. 2020), but as it is tidally locked, the dayside can reach temperatures up to $T_{\text{dayside}} \sim 2693$ K (Garhart et al. 2020). At a radius of $1.83 R_{\text{Jup}}$ and a mass of $0.92 M_{\text{Jup}}$, WASP-76 b is a benchmark UHJ that has been frequently investigated in recent years. Several atomic, ionised and molecular species have been detected in the atmo-

sphere of WASP-76 b, which are summarised in Table 2. Furthermore, this exoplanet has been the target of phase curve observations (Tsiaras et al. 2018; Garhart et al. 2020; May et al. 2021; Fu et al. 2021; Demangeon et al. 2024) and global circulation models (GCMs) have been developed to explain the observed signatures and better understand the mechanics of this atmosphere (e.g. May et al. 2021; Savel et al. 2022; Wardenier et al. 2021, 2023; Schneider et al. 2022; Beltz et al. 2022b,a, 2023; Sainsbury-Martinez et al. 2023; Demangeon et al. 2024).

In particular, the detection of Fe I by Ehrenreich et al. (2020) motivates our work. The authors first reported an asymmetrical Fe I detection in the terminators of WASP-76 b, when analysing high-resolution transmission spectra from ESPRESSO¹ (Pepe et al. 2021). This finding was supported by Kesseli & Snellen (2021); Kesseli et al. (2022), and Pelletier et al. (2023), who independently recovered the asymmetrical signature. To explain why Fe I is observed on the evening limb but not on the morning limb, Ehrenreich et al. (2020) suggest that this species must condense as it crosses the colder nightside, and thus should exist in gaseous form on the dayside of WASP-76 b. Furthermore, Pelletier et al. (2023) also report a tentative detection of Fe II in transmission studies of the atmosphere. Thus we aim to determine whether iron, in both the neutral and ionised forms, is present on the dayside of this planet via emission spectroscopy.

To the extent of our knowledge, only one high-resolution emission study has been published for this target so far. Yan et al. (2023) analysed data from CRIRES+² (Dorn et al. 2023) and reported the detection of CO and weak H₂O emission features. The CO signature was slightly redshifted ($2.1^{+0.8}_{-0.7}$ km/s), whereas the H₂O signal had a small blueshift (-5^{+12}_{-10} km/s, though we note the large uncertainty). These emission lines confirmed the existence of a thermal inversion on the dayside of WASP-76 b, as had been suggested from previous low-resolution spaceborne observations (Edwards et al. 2020; May et al. 2021).

High-resolution spectroscopy has been proven fundamental in the endeavour of characterising atmospheres, as it allows us to distinguish a forest of individual lines in the spectra. Additionally, due to the different Doppler shifts of the stellar and planetary signal over time, we are often able to disentangle the stellar contribution from the planetary features in high-resolution data (Snellen et al. 2010). In some cases, the line strength is large enough to allow for the analysis of lines individually (Wytenbach et al. 2015; Allart et al. 2018; Seidel et al. 2019; Allart et al. 2023). However, for weaker spectral features, we can instead employ a cross-correlation function (CCF) to harvest the signal of multiple lines at once, instead of individually (e.g. Snellen et al. 2010; Brogi et al. 2012; Birkby et al. 2013; Hoeijmakers et al. 2015; Allart et al. 2017; Ehrenreich et al. 2020; Azevedo Silva et al. 2022; Prinoth et al. 2023). Since all the planetary lines are shifted by the same radial velocity (RV) value, the robustness of the CCF is enhanced, and so is the significance of the detections.

In this work, we present the first analysis of high-resolution emission spectra at visible wavelengths for WASP-76 b obtained with ESPRESSO at the Very Large Telescope (VLT). The main goal is to probe the existence of Fe I and Fe II in the exoplanet's dayside, which could be contributing to the inverted pressure-temperature (P-T) profile. The thermal inversion layer has been previously confirmed in Yan et al. (2023) from H₂O emission

* Based on Guaranteed Time Observations collected at the European Southern Observatory under ESO programmes 1104.C-0350(U) and 110.24CD.004 by the ESPRESSO Consortium.

** Trottier Postdoctoral Fellow

¹ Echelle SPectrograph for Rocky Exoplanets and Stable Spectroscopic Observations

² The CRYogenic InfraRed Echelle Spectrograph Upgrade Project

Table 1. Properties of the planet WASP-76 b and its stellar host.

Parameter	Symbol (unit)	Value	Reference
Star			
Right ascension	RA	01 h 46 m 31.9 s	Gaia Collaboration (2020)
Declination	DEC	+02° 42' 02.0"	Gaia Collaboration (2020)
V magnitude	V-mag (mag)	9.52 ± 0.03	Høg et al. (2000)
Spectral type		F7	West et al. (2016)
Effective temperature	T _{eff} (K)	6329 ± 65	Ehrenreich et al. (2020)
Radius	R _* (R _☉)	1.458 ± 0.021	Ehrenreich et al. (2020)
Mass	M _* (M _☉)	1.756 ± 0.071	Ehrenreich et al. (2020)
Gravity	log g	4.196 ± 0.106	Ehrenreich et al. (2020)
RV semi-amplitude	K _* (m/s)	116.02 ^{+1.29} _{-1.35}	Ehrenreich et al. (2020)
Systemic velocity	v _{sys} (km/s)		
Epoch I		-1.2113 ± 0.0003	this work
Epoch II		-1.2134 ± 0.0003	this work
Epoch III		-1.2064 ± 0.0002	this work
Epoch IV		-1.2100 ± 0.0003	this work
Planet			
Radius	R _p (R _{Jup})	1.854 ^{+0.077} _{-0.076}	Ehrenreich et al. (2020)
Mass	M _p (M _{Jup})	0.894 ^{+0.014} _{-0.013}	Ehrenreich et al. (2020)
Planet surface gravity	g _p (m/s ²)	6.4 ± 0.5	Ehrenreich et al. (2020)
Inclination	i (deg)	89.623 ^{+0.014} _{-0.013}	Ehrenreich et al. (2020)
Semi-major axis	a (AU)	0.0330 ± 0.0002	Ehrenreich et al. (2020)
Orbital period	P (days)	1.80988198 ^{+0.00000064} _{0.00000056}	Ehrenreich et al. (2020)
Mid-transit time	T _c (BJD)	58080.626165 ^{+0.000418} _{0.000367}	Ehrenreich et al. (2020)
RV semi-amplitude	K _p (km/s)	196.52 ± 0.94	Ehrenreich et al. (2020)
Equilibrium temperature	T _{eq} (K)	2228 ± 122	Ehrenreich et al. (2020)
Dayside temperature	T _{day} (K)	2693 ± 56	Garhart et al. (2020)

lines, but observing the emission features of iron can help further constrain the thermal structure of the planet's dayside.

This paper is structured as follows: in Sect. 2, we describe the details of our observations; in Sect. 3, we present the data reduction, processing, and analysis steps for computing the CCFs; in Sect. 4, we report the results of the analysis; we compare our findings to the literature in Sect. 5 and propose an atmospheric scenario that could link our results with those from the literature; finally, we summarise and conclude in Sect. 6.

2. Observations

2.1. ESPRESSO spectroscopic data

The WASP-76 system was observed on four different epochs, two of them covering phases before the planet's secondary transit (2021 September 9 and 2022 October 14) and two after (2021 September 2 and 2022 October 18). The data were obtained with the ESPRESSO spectrograph (Pepe et al. 2021) installed at the VLT, at Cerro Paranal, as part of the programmes 1104.C-0350(U) and 110.24CD.004 of the Guaranteed Time Observation. The ESPRESSO mode was set to HR21 (1 unit telescope, 2 × 1 binning), with resolving power of R ~ 140 000. Fibre A was pointed to our target whereas Fibre B was pointing towards the sky to allow for sky subtraction. Each spectrum covers the visible wavelength range from ~3800 Å to ~7880 Å.

This resulted in a total of 148 high-resolution spectra, evenly split between the pre- and post-eclipse observations (74 spectra probing each phase range). The observations lasted between 3.5 h and 3.75 h for each epoch, with the individual exposure time set to 300 seconds. The left panel of Fig. 1 illustrates the orbital phases covered by the observations. We label each epoch

as data sets I, II, III, and IV, in order of increasing orbital phase at the start of observations. The right panels of this figure show the variation of airmass in each epoch, as well as the signal-to-noise ratio (S/N) of each data set (taken from order 106 of ESPRESSO, at wavelength ~ 5800 Å). The observation logs are summarised in Table 3.

2.2. EulerCam photometric data

We searched for potential photometric variability around the time of the ESPRESSO observations to rule out the presence of strong active regions on the star that could contaminate the retrieved emission spectrum. For this, we observed WASP-76 with EulerCam (Lendl et al. 2012), a 4k × 4k CCD detector installed at the Cassegrain focus of the 1.2-m *Leonhard Euler* Telescope at ESO's La Silla Observatory. We monitored the star every third night in two different monitoring campaigns: i) from 2021 June 20 to 2022 January 20, and ii) from 2022 October 1 to 2023 January 10. Each monitoring observation involved taking a sequence of six images in five different filters, with exposure times indicated in parenthesis: Johnson-B (60 s), Johnson-V (30 s), Sloan-r' (20 s), Sloan-i' (30 s) and Sloan-z' (40 s).

The raw full-frame EulerCam images for each night of observation are corrected for over-scan, bias and flat-field using the standard reduction pipeline (Lendl et al. 2012). The aperture photometry is performed using circular apertures with radii ranging from 16 to 80 pixels, placed on the target star and three bright stars in the field of view. To mitigate the changing position of stars on the detector, the placement of apertures was performed using their astrometric solution (Lang et al. 2010). The optimal aperture for each night is found by minimising the

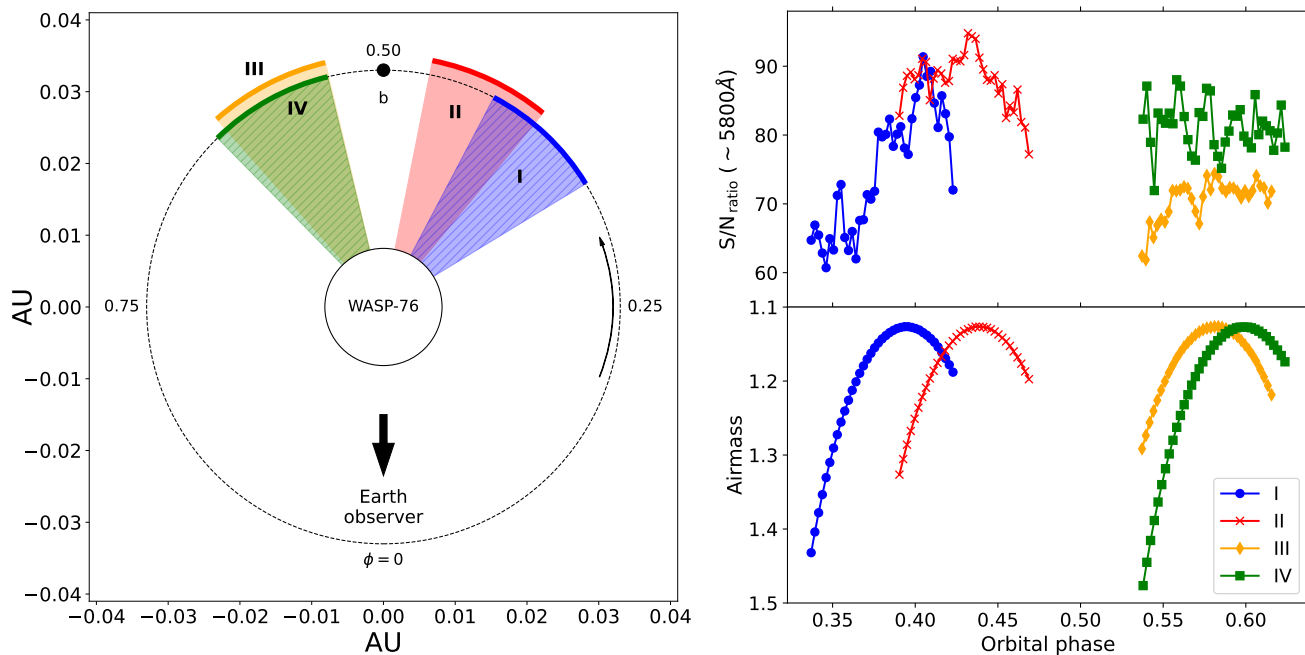


Fig. 1. Details of the observations of WASP-76 b with ESPRESSO. **Left:** Orbital diagram of WASP-76 b showing the epochs and phases (ϕ) during which the system was observed. The curved arrow indicates increasing orbital phase for the planet. **Right:** Variation of signal-to-noise ratio around 5800 Å (*top*) and airmass (*bottom*) for each epoch observed. See more details in Table 3.

photometric scatter of the consecutive images. The light curves from Johnson-*B* and Sloan-*z'* were removed as they suffered from strong systematics. The normalised differential light curves for Johnson-*V*, Sloan-*r'*, and Sloan-*i'* are shown in Fig. 2.

WASP-76 appears to be photometrically quiet around the ESPRESSO eclipse observations, with upper limits on the flux variability from the light curves being 4.95 mmag (*V*), 7.17 mmag (*r'*), and 5.55 mmag (*i'*). We note that our observations cannot resolve the two components of the WASP-76 binary system (Wöllert & Brandner 2015). The companion star, WASP-76 B, is likely a late-G or early K-type dwarf (Ehrenreich et al. 2020), and it lies at a separation of $\sim 0.44''$, which corresponds to 53.0 ± 8.8 AU (Ginski et al. 2016; Ngo et al. 2016; Bohn et al. 2020). Though the stars are unresolved, our analysis indicates no photometric activity in general, which would suggest both components A and B are quiet.

3. Analysis

3.1. Reducing ESPRESSO data and extracting planet's spectra

The raw data were reduced with the ESPRESSO Data Reduction System (DRS, version 3.0.0, Pepe et al. 2021). We proceeded to analyse the S1D sky-subtracted spectra produced by this pipeline, which is in the rest frame of the barycenter of the Solar System. In S1D, all orders of the spectrograph have been merged into a single 1D spectrum for each exposure. Our analysis follows a similar procedure to previous works, and its seven steps are detailed below:

- Remove telluric contamination.

We removed the telluric contamination using Molecfit (version 4.2, Smette et al. 2015; Kausch et al. 2015) with the ESPRESSO settings. In some regions of the spectra, the telluric features are completely saturated, which makes it impossible to apply a correction. In the following wavelength

ranges (in air), we could not achieve a satisfactory correction and thus they are masked at later stages when calculating the CCF: [5867.56 – 6005.55] Å, [6270.23 – 6344.15] Å, [6439.08 – 6606.96] Å, [6858.15 – 7417.40] Å, [7586.03 – 7751.12] Å.

- Normalise spectra.

The continuum contribution was removed from the spectra with RASSINE (Cretignier et al. 2020), via the S-BART Python package (Silva et al. 2022), which optimises the process for ESPRESSO data. This step removes the interference patterns that have been reported to affect the continuum of ESPRESSO observations (commonly referred to as wiggles).

- Fit for the systemic velocity.

We found that there was a discrepancy in the systemic velocity (v_{sys}) values presented in the literature. The discovery paper reports this value as -1.0733 ± 0.0002 km/s (West et al. 2016); SIMBAD gives -1.152 ± 0.0033 km/s, from the Gaia Data Release 2 (Soubiran et al. 2018); and the analysis of Ehrenreich et al. (2020) states different values for each epoch observed: -1.162 , -1.167 , and -1.171 km/s (with typical uncertainty of the order of 0.002 km/s). This value warrants attention as it is an important parameter to accurately shift the spectra between the different rest frames. Thus we chose to perform a simple least-squares fit of a Keplerian to the RV values calculated by the pipeline, setting v_{sys} as the only free parameter (the remaining orbital elements were set to those reported in Table 1). We obtained four values of v_{sys} : -1.2113 , -1.2134 , -1.2064 , -1.2100 km/s, for epochs I, II, III, and IV, respectively. The typical uncertainty obtained from this fit is of the order of 0.0003 km/s, though the real uncertainty on v_{sys} is expected to be much greater. In the following steps, the data of each epoch was processed using the corresponding v_{sys} retrieved here.

- Create stellar template.

All of the spectra were shifted to the stellar rest frame and the median spectrum was computed for each epoch inde-

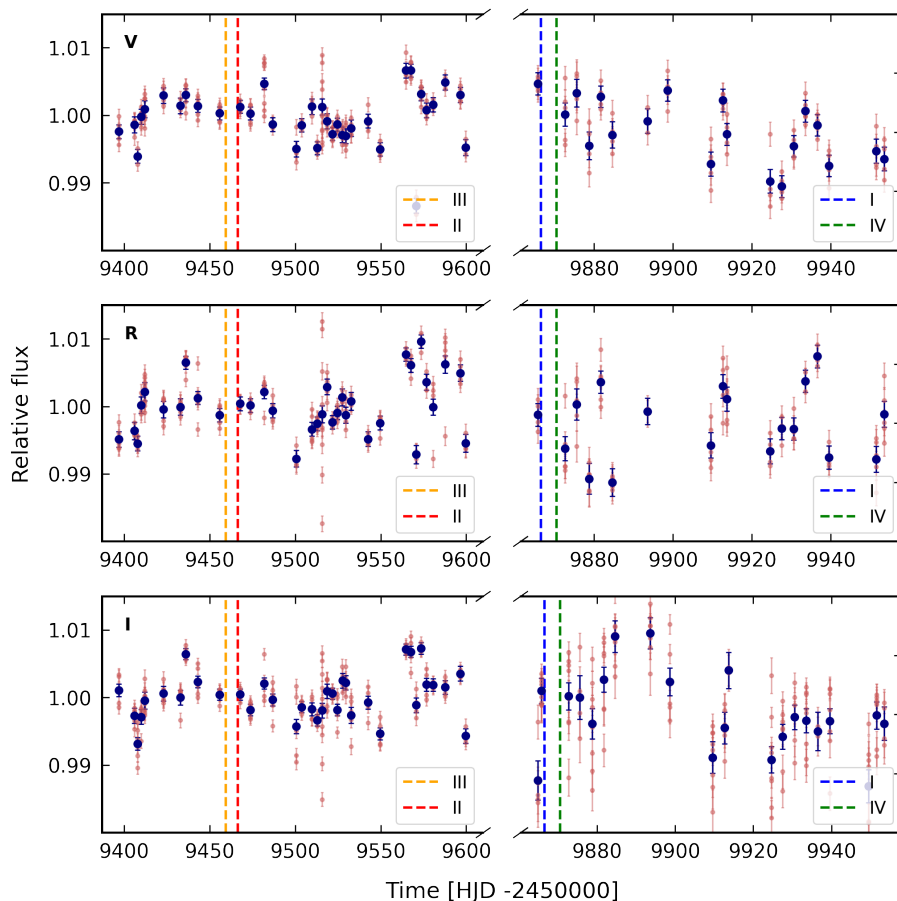


Fig. 2. Photometric monitoring of WASP-76: EulerCam light curves in Johnson-V (top), Sloan- r' (middle), and Sloan- i' (bottom) filters, unbinned (red) and binned per day (blue). WASP-76 can be considered photometrically quiet around the time of the ESPRESSO observations (vertical dashed lines).

pendently. The median spectra contain only the stellar lines, which are aligned at the same position in the star’s rest frame, increasing their signal. The planetary lines are very faint and their position on the spectra changes significantly over time (the planet’s RV changes by ~ 2.4 km/s between the start of two consecutive exposures). Thus their contribution is diluted when computing the median template in the stellar rest frame, averaging out to values comparable to the noise.

– Extract planet’s spectra.

To obtain spectra that contain only the planetary features, we interpolate all spectra to a common wavelength grid and subtract the stellar median template from every spectrum of the corresponding epoch, in the stellar rest frame.

– Compute cross-correlation.

We compare each exposure of the planetary spectra with synthetic models created with `petitRADTRANS` (Mollière et al. 2019, 2020; Alei et al. 2022, see next section), by computing a non-weighted CCF according to:

$$\text{CCF}(\text{RV}) = \sum_i s_i m_i(\text{RV}) \quad (1)$$

where s_i is each data point in the planet’s spectrum, and $m_i(\text{RV})$ is each data point of the model shifted by a given RV lag. At this stage, each spectrum produces one CCF curve, with velocities ranging from -300 to 300 km/s, with a step of 1 km/s.

– Co-add CCFs in the planet rest frame.

The last step is to shift the individual CCFs to the planetary rest frame, sum them, and assess if there is a detection. The planetary signal has a small amplitude in the individual

CCFs, but given that the CCF peaks are expected to align when working in the planet’s rest frame, then the summation can provide detections at a higher confidence level. We shift the CCFs according to the Keplerian motion of the planet, computed using the parameters shown in Table 1. Our analysis is twofold: firstly, we analyse the co-added CCF resulting from each independent epoch (we combine the 39 CCFs of epoch I into one, the 35 CCFs of epoch II into one, and so on); secondly, we construct a co-added CCF without the separation of epochs, so we combine the 148 CCFs into one. A detection of emission lines will manifest itself as a positive peak at (or close to) $\text{RV} = 0$ km/s, since we are analysing it in the planet’s rest frame.

3.2. Synthetic models for CCF

The synthetic models to which we compared the observations were produced with the Python package `petitRADTRANS` (version 2.7.7) (Mollière et al. 2019, 2020; Alei et al. 2022), which can calculate both transmission and emission spectra of exoplanets. We chose the high-resolution mode (“lbl”, $\lambda/\Delta\lambda = 10^6$) to better match our observations, and created separate emission templates with the spectral lines of Fe I and Fe II (opacities were contributed to `petitRADTRANS` by K. Molaverdikhani³, calculated from the line lists of R. Kurucz⁴). We set the planetary parameters to those of WASP-76 b, assuming a hydrogen-helium

³ https://petitradtrans.readthedocs.io/en/latest/content/available_opacities.html#contributed-atom-and-ion-opacities-high-resolution-mode

⁴ <http://kurucz.harvard.edu/>

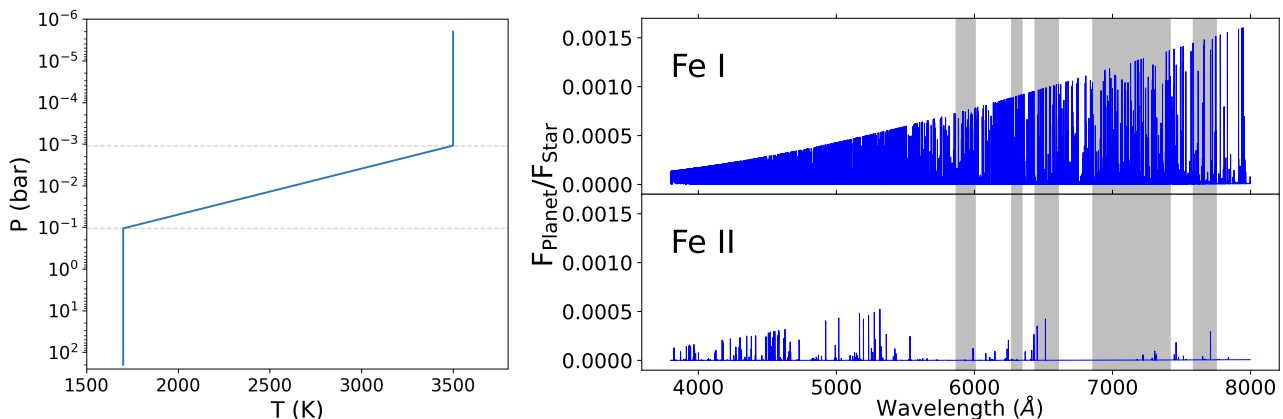


Fig. 3. Details of models created for the CCF computation. **Left:** Pressure-temperature (P-T) profile assumed for the dayside of WASP-76 b to create the templates of Fe I and Fe II, hereafter PT01 (see Sect. 3.2), based on the GCM work of Wardenier et al. (2021, 2023). **Right:** petitRADTRANS models for Fe I (top) and Fe II (bottom), assuming the thermal profile PT01. The shaded regions are excluded from the CCF calculation due to telluric residuals on the empirical spectra.

Table 2. Literature reports of atom, ion, and molecule detections in the atmosphere of WASP-76 b.

Chemical species	Reference
Ba II	[1], [2]
Ca I	[2]
Ca II	[1], [2], [3], [4], [5], [6], [7]
Co I	[6]
Cr I	[1], [2], [6], [7]
Fe I	[1], [2], [3], [6], [7], [8], [9]
Fe II	[2]
H I	[1], [2], [6]
He I	[4], [10]
K I	[2], [3], [6], [7]
Li I	[1], [2], [3], [6], [7]
Mg I	[1], [2], [3], [6]
Mn I	[1], [2], [3], [6]
Na I	[1], [2], [3], [5], [6], [7], [11], [12], [13], [14]
Ni I	[2], [6]
O I	[2]
Sr II	[6]
V I	[1], [2], [6], [7]
CO	[15], [16]
H ₂ O	[15], [16], [17], [18], [19], [20]
HCN	[17]
OH	[21]
TiO	[15], [18], [22]
VO	[2], [18], [20]

References. (1) Azevedo Silva et al. (2022); (2) Pelletier et al. (2023); (3) Tabernero et al. (2021); (4) Casasayas-Barris et al. (2021); (5) Deibert et al. (2021); (6) Kesseli et al. (2022); (7) Deibert et al. (2023); (8) Ehrenreich et al. (2020); (9) Kesseli & Snellen (2021); (10) Lampón et al. (2023); (11) Seidel et al. (2019), (12) Žák et al. (2019), (13) Seidel et al. (2021), (14) Kawauchi et al. (2022), (15) Fu et al. (2021), (16) Yan et al. (2023), (17) Sánchez-López et al. (2022), (18) Tsiaras et al. (2018), (19) Fisher & Heng (2018), (20) Changeat et al. (2022), (21) Landman et al. (2021), (22) Edwards et al. (2020).

atmosphere with iron as the only trace species. We set both the Fe I and Fe II abundances to be the solar abundance of Fe I (Lodders 2020), keeping this value constant in every layer of the

atmosphere. The P-T profile was based on the GCM work of Wardenier et al. (2021, 2023) (shown in Fig. 3). We define a two-point model, where the deep and outer atmospheres are represented by isotherms at 1700 K and 3500 K, respectively. The inversion layer is described by a gradient between 1 – 100 mbar that connects the two isotherms. At a later stage, we diverge from this model and define new atmospheric profiles to evaluate the effect it has on the CCF signature.

The package `petitRADTRANS` provides spectra in units of spectral flux density ($\text{erg cm}^{-2} \text{s}^{-1} \text{Hz}^{-1}$). We transform them into contrast models ($F_{\text{planet}}/F_{\text{star}}$) by multiplying by the area of the planet disk and dividing by the flux of the star (modelled as a blackbody with $T_{\text{eq}} = 6329 \text{ K}$). Figure 3 displays the models of Fe I and Fe II used in the CCF calculations. The models are interpolated to the same wavelength grid as the observations when computing the CCFs.

4. Results

The resulting CCFs for neutral and ionised iron are presented in Fig. 4. In the top panels, the CCFs have been co-added in the planet’s rest frame for each epoch, calculating the RV shift with the Keplerian solution defined using the parameters presented in Table 1. The CCFs were then converted into a S/N scale by calculating the standard deviation of the baseline (between $[-115, -35] \text{ km/s}$ and $[35, 115] \text{ km/s}$) and dividing everything by this measurement. Furthermore, we fit a simple 1D Gaussian curve locally around zero to retrieve the RV value of the signature. In the middle panels, we show the CCF resulting from adding all curves from the four epochs in the planet’s rest frame (normalised by the baseline after the summation), also fitted with a Gaussian curve. Lastly, in the bottom panels, we produce the $K_p - v_{\text{sys}}$ plot. For this, we add all 148 CCFs in the planet’s rest frame, but for each row of the plot, we compute the Keplerian solution assuming a different value for the semi-amplitude velocity, K_p (all other parameters remain constant, see Table 1). If the theoretical orbital parameters are correct and no atmospheric dynamics are detectable in the exoplanet, we should expect a detection at the intersection of $K_p = 196.52 \text{ km/s}$ and $v_{\text{sys}} \sim -1.2 \text{ km/s}$ (traced by the dashed lines in the figure).

Table 3. Observation logs.

Data set	Night	VLT Unit	# spectra	Airmass range	Exposure time	Phase coverage	S/N range*
I	2022-10-14	UT1	39	1.13 – 1.43	300 s	0.34 – 0.42	61 – 91
II	2021-09-09	UT2	35	1.13 – 1.33	300 s	0.39 – 0.47	77 – 94
III	2021-09-02	UT1	35	1.13 – 1.29	300 s	0.54 – 0.61	62 – 74
IV	2022-10-18	UT1	39	1.13 – 1.48	300 s	0.54 – 0.62	72 – 88

Notes. * Values taken from order 106 of ESPRESSO, at $\sim 5800\text{\AA}$.

Table 4. Results from the Gaussian fits to the CCFs.

Species	Epoch	Detection	S/N	RV peak (km/s)	FWHM (km/s)
Fe I	I	yes	3.1σ	-4.8 ± 0.3	6.3
	II	tentative	1.8σ	-8.0 ± 0.9	13.5
	III	tentative	2.4σ	-4.5 ± 0.5	8.8
	IV	tentative	2.4σ	-1.3 ± 0.8	14.8
	I & II (pre-eclipse)	yes	3.8σ	-6.0 ± 0.4	9.4
	III & IV (post-eclipse)	yes	3.5σ	-3.3 ± 0.5	11.9
	Four epochs co-added	yes	6.0σ	-4.7 ± 0.3	10.6
Fe II	I, II, III, IV	no	-	-	-

4.1. Detection of blueshifted Fe I in emission

We report a 3.1σ detection of Fe I in epoch I, and tentative detections in epochs II, III, and IV, with significances of 1.8σ , 2.4σ , and 2.4σ , respectively. The S/N of these detections is rather low, and other peaks are visible in the co-added CCFs. Some of these peaks lie slightly above what could be considered the noise level, at values distant from the zero-velocity point. The CCF process itself can introduce artefacts resembling detection peaks when lines from the template randomly match with the empirical features of other species scattered throughout the planet’s spectra (Borsato et al. 2023). However, in this case, it seems that the noise in the continuum is mostly dominated by red noise.

The weakest detection of the individual epochs comes from epoch II, which is puzzling at first because these observations had the best seeing conditions of the four epochs observed, and the spectra have the best S/N. However, this was the only epoch observed with UT2 of the VLT, whereas UT1 was used for the other epochs. UT2 tends to be more affected by the interference pattern created in ESPRESSO (wiggles), therefore the correction of this effect might have left more residuals compared to the other epochs, in turn leading to a less significant detection. Prinoth et al. (2023) reported similar quality issues between data from UT1 and UT2 (see their Appendix A).

When combining all epochs, the neutral iron detection is much clearer, at a S/N of 6.0σ (see Fig. 4). Table 4 summarises the significance of our findings. Lastly, in the $K_p - v_{\text{sys}}$ plot (Fig. A.1), Fe I is detected at the expected K_p value, with a blueshifted v_{sys} , and no other strong peaks are found in the explored parameter space. The detection of emission lines confirms the existence of a thermal inversion layer in the dayside of WASP-76 b. The inversion had been previously hinted at by Edwards et al. (2020); May et al. (2021); Fu et al. (2021), and confirmed by Yan et al. (2023) using near-infrared CRIRES+ emission spectroscopy. Our data support their findings.

Furthermore, we report that our Fe I detection is blueshifted with respect to the planetary rest frame. The CCF for the four epochs produces a peak at an RV of -4.7 ± 0.3 km/s (full width at half maximum, FWHM, of 10.6 km/s). For the co-added CCFs of each epoch, the Gaussian fits are centred at -4.8 ± 0.3 , -8.0 ± 0.9 , -4.5 ± 0.5 , and -1.3 ± 0.8 km/s, with FWHM values

of 6.3, 13.5, 8.8, and 14.8 km/s, respectively for epochs I, II, III, and IV (see Fig. 4). We note that there is some scatter in the RV shift observed from epoch to epoch, though it is unclear if the differences are caused by the low S/N of the planetary signature or if they indicate a physical variation of the atmosphere. Moreover, our uncertainties are likely underestimated as they represent only the nominal error of the Gaussian fit. It is difficult to properly account for the uncertainties created by the correlated noise of the CCF. Notwithstanding, all the observations presented have clear blueshifted peaks that are identified consistently across the epochs. There seems to be a drift of ~ 3 km/s between the observations of 2021 (II and III) and 2022 (I and IV) for the same phases. However, it is not possible to draw any significant conclusions at this point. In Fig. 5, we present the combined CCFs by phase range, for pre- or post-eclipse. The observations after the eclipse reveal a smaller shift, -3.3 ± 0.5 km/s (FWHM = 11.9 km/s) than those obtained before the eclipse, -6.0 ± 0.4 km/s (FWHM = 9.4 km/s). The observations of epochs I and II (pre-eclipse) only overlap partially in phase coverage, so this could indicate a gradual change as the planet rotates. However, even with epochs covering very similar phase ranges, such as epochs III and IV, the RV peaks of their CCFs are discrepant at the 5σ level. The Gaussian fits on epochs I (pre) and III (post) show less broadening than for II (pre) and IV (post), so we consider the fits of I and III to be more significant than their counterparts at the same phase. This implies a consistent blueshift in the emission signal from both the east and west dayside hemispheres of WASP-76 b of about -4.6 km/s (see Fig. 4). Overall, further observations would be useful to confirm if these velocity discrepancies are the result of physical processes, and to shed more light on what could be causing them.

We considered if adopting an eccentric orbit, instead of a fully circular orbit, would alter the results and eliminate the blueshift. Given the age of the system (1.8 Gyr, Ehrenreich et al. 2020), we expect the orbit to have circularised (see favourable arguments for this orbital solution in Ehrenreich et al. 2020, Methods, but see also Valente & Correia 2022). Thus we assumed $e = 0$ in the calculations described so far. However, a slightly eccentric orbit might perhaps explain this signature. Furthermore, Savel et al. (2022) reported that allowing for a small eccentric-

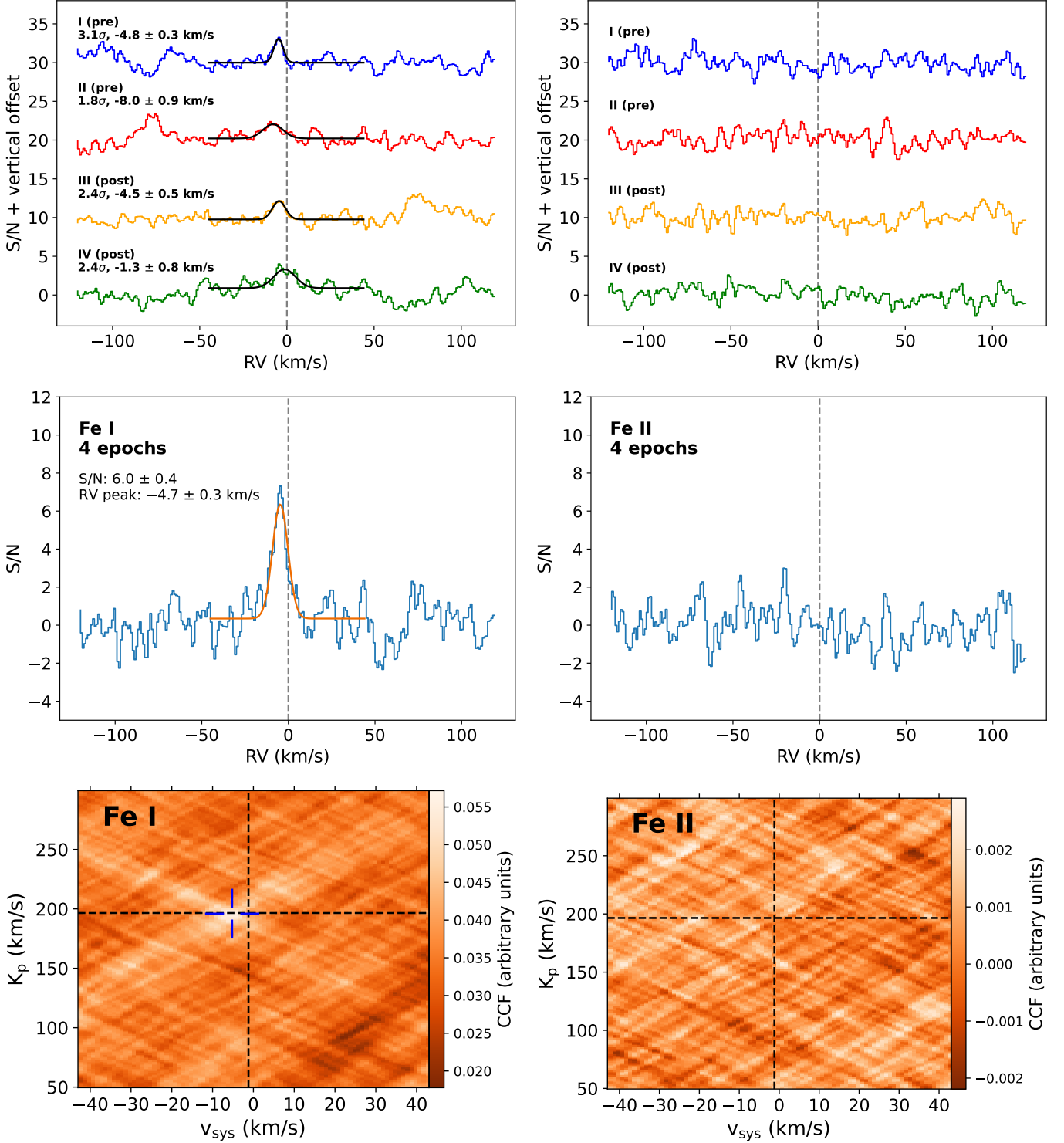


Fig. 4. Results of the CCF analysis for Fe I (*left*, detection) and Fe II (*right*, non-detection). **Top:** Summed CCFs in the planet rest frame, separated by epoch, with 1D Gaussian fits (black lines). Fe I is tentatively detected at a 2–3 σ level in each epoch and all epochs show a blueshifted signal. **Middle:** Summed CCFs of the four epochs in the planet rest frame, with no epoch separation. Fe I shows a 6.0 σ detection, as traced by the 1D Gaussian fit (black line). **Bottom:** $K_p - v_{\text{sys}}$ plot of the four epochs combined (see Fig. A.1 for the individual epochs). The black dashed lines indicate the expected position of the signal. The location of the strongest signal is pinpointed by the blue dashes, for the case of Fe I.

ity of 0.01 was a necessary adjustment to reproduce the transit signature of Fe I in WASP-76 b (Ehrenreich et al. 2020), combined with high-altitude, optically thick clouds of Fe I, Al₂O₃, and Mg₂SiO₄. So we investigated the possibility of WASP-76 b having an eccentric orbit.

The phase curve of WASP-76 b was recently observed with CHEOPS⁵ (Demangeon et al. 2024). These authors placed an upper limit on the eccentricity of $e = 0.0067$. We set the eccentricity to this upper limit, computed the CCFs with the newly shifted

⁵ CHAracterising ExOPlanets Satellite

spectra, and compared the two cases. In Fig. 6, we present the co-added CCFs for the cases of $e = 0$ and $e = 0.0067$. The change in RV of the CCF peaks of individual epochs is between 0 km/s and 3 km/s (top panel), with the peak in epochs I and II being less blueshifted compared to the zero-eccentricity case, and epochs III and IV being more blueshifted. When all CCFs are co-added (bottom panel), the change is negligible. As the blueshift remains present in all cases, we rule out the possibility that this signature is due to unaccounted-for eccentricity. In Sect. 5, we discuss further possible origins for the blueshifted Fe I.

4.2. Non-detection of Fe II in emission

We did not detect the presence of Fe II, even when adding the 148 CCFs from all epochs (see right panels of Fig. 4). Fe II has been detected in several UHJs via transmission spectroscopy, thus it is expected to be present on the daysides of these planets. However, it is expected to be more abundant at high altitudes, where Fe I is ionised by the hotter temperatures. These atmospheric layers are more challenging to probe with emission spectroscopy due to being more optically thin. Thus it is not surprising we could not detect Fe II emission on WASP-76 b, even if we expect it to be present.

4.3. Constraining P-T profile

Once we had confirmed the presence of Fe I in emission, we investigated how changes in the P-T profiles would affect the CCF peak. Thus we defined ten different P-T profiles, computed the synthetic template with `petitRADTRANS`, and calculated the cross-correlation for all epochs. Starting from the initial P-T profile (PT01, see Fig. 3 and Sect. 3.2, Wardenier et al. 2021, 2023), we modified either the temperature of the lower layer of the atmosphere, the temperature of the upper layer, the pressure boundaries of the inversion layer, or a combination of these. The characteristics of each P-T profile are shown in the bottom left panel of Fig. 7 and listed in Table B.1. The corresponding synthetic templates that were utilised for the CCF can be found in Fig. B.1. Despite the fact the Fe I opacities in `petitRADTRANS` were only calculated for temperature values up to 4000 K, we decided to go above this value in some of the P-T profiles. This means that the opacities used by `petitRADTRANS` when $T > 4000$ K are the same ones as for $T = 4000$ K. However, the radiative source function and the atmospheric scale height are not constant for temperature values that extend beyond the pre-defined P-T grid, thus they still hold some useful information.

We co-added the 148 CCFs corresponding to each P-T template (top panel of Fig. 7) and fitted the resulting peaks with Gaussian curves. The Fe I detection can be found in all tested profiles except for PT02, which corresponds to the profile with the inversion temperature located deep in the atmosphere. As expected, the significance of the detection changes in the different cases, with the weakest detection stemming from PT05, another profile that assumes the inversion temperature deeper in the atmosphere, though not as deep as for PT02.

Modifying the temperature of the lower or upper layers seems to have a limited impact on the significance, as the values only increase or decrease slightly compared to the base model PT01. The case that produces the strongest detections is the one where the temperature of the lower layer was reduced to $T_{\text{inner}} = 1200$ K.

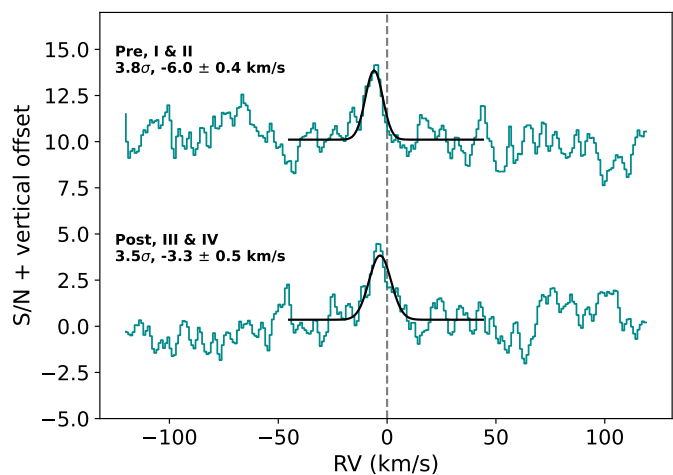


Fig. 5. Summed CCF curves of the epochs before the eclipse (top) and after (bottom). The Fe I signal is more blueshifted in phases before the eclipse, and becomes less blueshifted after.

A further visual investigation of the models revealed that many lines were saturated. This is likely due to the cut-off temperature defined for the isotherm at lower pressures. Strong lines that reach the blackbody curve defined by this isotherm thus have the same brightness temperature and appear saturated. In principle, if the lines were not saturated, the significance of the Fe I detection would change, but it would not alter our ultimate scientific conclusion that neutral iron is detected on WASP-76 b.

5. Discussion

5.1. Blueshifted Fe I emission

The Fe I emission signature we report on the dayside of WASP-76 b is blueshifted by ~ -4.7 km/s. Similar blueshifted signals have been identified in recent works, such as in CO and H₂O in WASP-77A b (Line et al. 2021), and H₂O in our target, WASP-76 b (Yan et al. 2023). However, the mechanism behind them has not been investigated so far.

The Doppler shift observed here cannot be explained by an eccentricity of the orbit, which is very close to zero (see Sect. 4.1). It also does not trace solely the day-to-night wind proposed in recent transmission studies (Seidel et al. 2019, 2021; Ehrenreich et al. 2020), which would appear redshifted in dayside observations (in the planet rest frame). Moreover, this wind is seen at the atmospheric limbs with transit spectroscopy, whereas our observations are most sensitive to integrated dayside emission. It seems to require that additional components be added to the atmospheric dynamics scenario, to ensure that the final disk-integrated signature is blueshifted. In this section, we propose a simple scenario of atmospheric circulation that could explain our observations, and we illustrate the proposed dynamics of the planet’s atmosphere in Fig. 8.

Our interpretation is that material on the dayside of WASP-76 b is moving towards the observer, with similar magnitude on both the east and west hemispheres. The day-to-night heat redistribution pattern proposed by GCMs for UHJ in the presence of drag (e.g. Wardenier et al. 2021) would have an RV component close to zero at orbital phases close to the eclipse, when the day-side disk is almost perpendicular to the observer’s perspective.

In emission spectroscopy, observations are more sensitive to the hottest region of the dayside, in the vicinity of the substellar

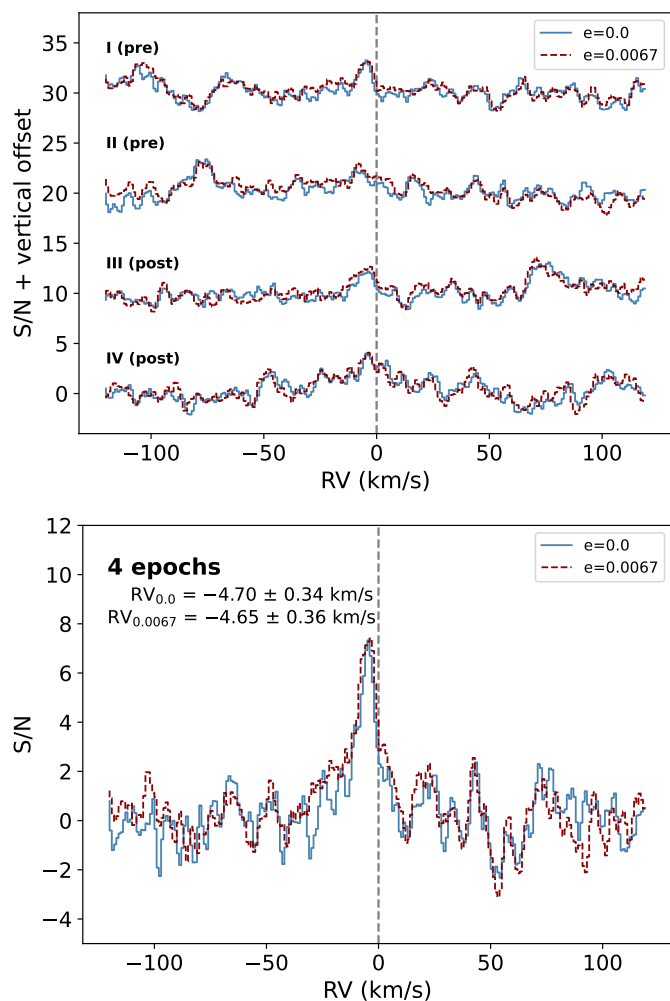


Fig. 6. CCFs of Fe I calculated for the cases of $e=0$ and $e=0.0067$ (CHEOPS upper limit, Demangeon et al. 2024). The CCFs in the top panel are separated by epoch, and the differences in the RV peaks between these eccentricity scenarios are between 0 and 3 km/s. In the bottom panel, all epochs are co-added, and the difference between the two peaks is negligible. Assuming a slightly eccentric orbit, rather than a circular orbit, does not eliminate the blueshifted signature seen for Fe I.

point. As such, we could be detecting Fe I atoms that are rising in the atmosphere, in a radial motion from the inner to the outer atmospheric layers. This displacement is possibly generated by the hotspot at or close to the substellar point. A series of works by Seidel et al. (2019, 2020, 2021) has shown that vertical upwards winds in the upper atmosphere of UHJs, including WASP-76 b, were the likely cause for the broadening observed in the Na I doublet, being of the order of 20 km/s. Moreover, if these hotter parcels of atmosphere are transported from the dayside to the nightside of the planet, via the day-to-night wind or the super-rotating equatorial jet, the atoms would be detectable at the terminator via transmission spectroscopy, as was reported by Ehrenreich et al. (2020); Kesseli & Snellen (2021); Kesseli et al. (2022); Pelletier et al. (2023). Furthermore, if these atoms condense when reaching the nightside, due to the cooler temperatures, it could explain the glory effect reported by Demangeon et al. (2024) from the light curve analysis.

This could mean that the hotspot is generating the upward displacement of a substantial amount of Fe I atoms. Sainsbury-Martinez et al. (2023) investigated GCMs models that included

vertical transfer of heated material in the outer atmosphere of UHJs. They concluded that the differences between the day and nightside temperatures ultimately lead to transport in the upward direction on the dayside, whereas the nightside sees a downward motion. However, these authors assumed a P-T profile that combined an adiabat for the deep atmosphere and an isotherm for the outer layers, with no inversion layer present. Had a thermal inversion been included, we do not know to what extent it would alter their findings.

As mentioned in the previous section, there is some doubt as to whether the changes in RV shift from one epoch to another are real, or if they are a product of the small S/N residual contamination from activity, or a combination of these, for example. How (or if) the magnitude of the shift varies can help us locate the hotspot of WASP-76 b. If we consider that the planetary signal is more blueshifted before the eclipse than after (see Fig. 5), that could mean the hotspot is shifted to the west. As exemplified in Fig. 8, a westward shift would create a stronger blueshift signature before the occultation. Whereas if we analyse the CCFs for each epoch separately, one can argue that the peaks on epochs II and IV have a less constrained fit than those of epochs I and III, thus we should only consider the two latter results in our discussion. In this case, the blueshift has the same magnitude across both phases, which can point to the lack of an offset for the hotspot. With a hotspot that is located at or close to the substellar point, observations before and after the occultation would reveal a mirrored wind structure and thus create a similar atmospheric RV shift overall. May et al. (2021) have reported a negligible offset of the hotspot for WASP-76 b, though this conclusion was drawn from Spitzer data which is potentially probing a different altitude in the atmosphere. Beltz et al. (2022b) show that the hotspot offset can be reduced as a result of applying more sophisticated active magnetic drag treatments over more approximate ones. This goes to show the importance of studying planetary magnetic fields and their impact on atmospheric circulation. On the other hand, Wardenier et al. (2021) and Savel et al. (2022) required a hotspot offset in their GCMs in order to reproduce the observational findings of transmission spectroscopy. More observations of the dayside of WASP-76 b with higher S/N and better time resolution are necessary to constrain the position of the hotspot.

To further dive into the atmosphere of WASP-76 b, it would be necessary to develop a retrieval framework, such as those presented in Brogi & Line (2019); Seidel et al. (2020, 2021); Pelletier et al. (2021); Gandhi et al. (2022), adapted to emission spectroscopy. Such a task is outside the scope of this paper. GCM studies are also an efficient tool to unravel the underlying atmospheric phenomena at play in the atmospheres of UHJs. Wardenier et al. (2021, 2023) have developed a 3D model for WASP-76 b, but have produced only the transmission spectra for comparison with the already published transit data (Ehrenreich et al. 2020). Producing GCM to delve into the scorching dayside of this planet is, likewise, not the goal of this observational paper, though we strongly encourage this effort.

5.2. Lack of Fe II detection

Fe II has only been detected in the dayside of one other UHJ, KELT-20 b/MASCARA-2 b (Borsa et al. 2022), and only in the post-eclipse data. Despite this, follow-up studies were not able to find its signature on the same planet (Yan et al. 2022; Kasper et al. 2023; Petz et al. 2024). A non-detection has also been reported for the dayside of KELT-9 b by Pino et al. (2020) and Ridden-Harper et al. (2023). Cont et al. (2022) did not detect

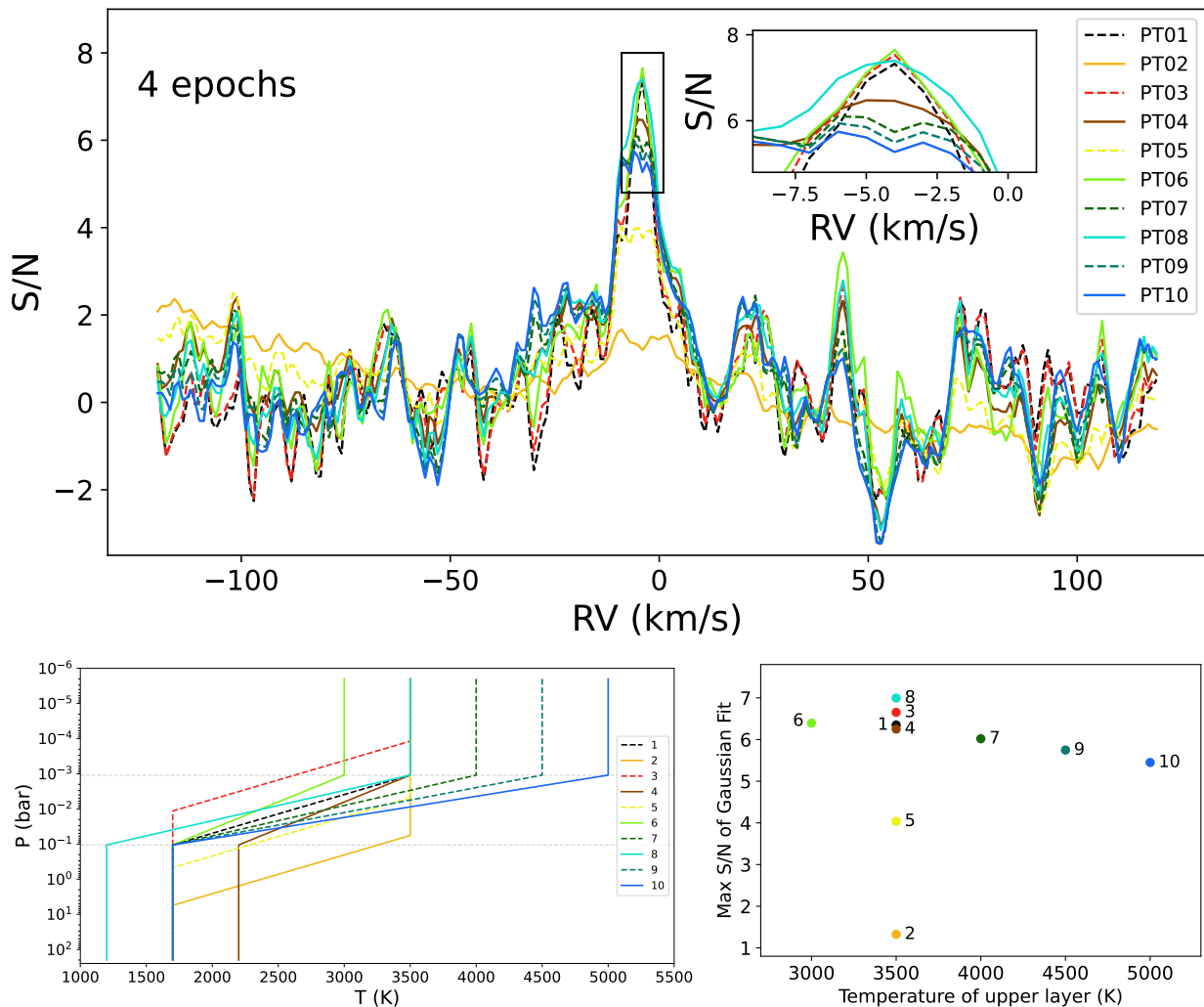


Fig. 7. Analysis of the dependence of the iron detection on the model used to compute the CCF. **Top:** Four-epoch co-added CCFs for Fe I computed with different templates that correspond to each P-T profile (bottom left panel). **Bottom left:** P-T profiles (see also Fig. B.1 and Table B.1). **Bottom right:** Maximum S/N value of Gaussian fit to co-added CCFs of four epochs, computed with the Fe I template corresponding to each P-T profile.

Fe II on the emission spectra of WASP-33 b, and their injection-recovery tests concluded that it would not be detectable in their data. For the case of WASP-121 b, a similar planet to WASP-76 b, it was observed with ESPRESSO in eight different epochs, producing about two times as much spectra than we analysed in this work (Hoeijmakers et al. 2024), but Fe II remained undetected in the dayside of this UHJ.

Fe I ionises at lower pressures and higher temperatures in the atmosphere, decreasing its abundance and increasing that of Fe II. However, the upper layers of the atmosphere are more optically thin. This is the reason why transmission spectroscopy is a better method to explore them and has been a more successful technique at finding Fe II. To probe Fe II at these pressures with emission spectroscopy, it would require a greater abundance of this ion, or a larger number of strong lines available to probe it. Our Fe II template in the optical regime contains ~ 1200 lines, which is one order of magnitude smaller than the ~ 11700 lines present in the Fe I template, a species that is more abundant further down in the atmosphere, and thus more amenable to be detected in thermal emission. The Fe II lines become stronger for UHJs with higher equilibrium temperatures, which might make this ion traceable. The aforementioned works investigated planets hotter than WASP-76 b, and did not report detections. With

WASP-76 b sitting on the colder edge of the UHJ temperature range, it is expected that we cannot prove the existence of Fe II on its dayside with CCF techniques.

The lack of confident detections or non-detections of Fe II does not allow for any meaningful conclusions regarding a population trend. We stress that it would be of great interest to trace the ionised state of iron as we expect it to be affected by planetary magnetic fields.

6. Summary and conclusions

We observed the dayside of the ultra hot Jupiter WASP-76 b with ESPRESSO on four different epochs. We collected a total of 148 high-resolution emission spectra. Half of these were obtained just before the planet’s secondary transit (phases 0.34 - 0.47), and the other half right after (0.54 - 0.62), providing insight into both the east and west hemispheres. This is the first emission spectroscopy study carried out for WASP-76 b at visible wavelengths. We also present monitoring data of WASP-76 from EulerCam, which shows that the host star (and its binary companion) are both quiet stars, with little photometric variation.

Our main goal was to detect Fe I and Fe II in emission on the dayside of WASP-76 b. We used the CCF method to compare

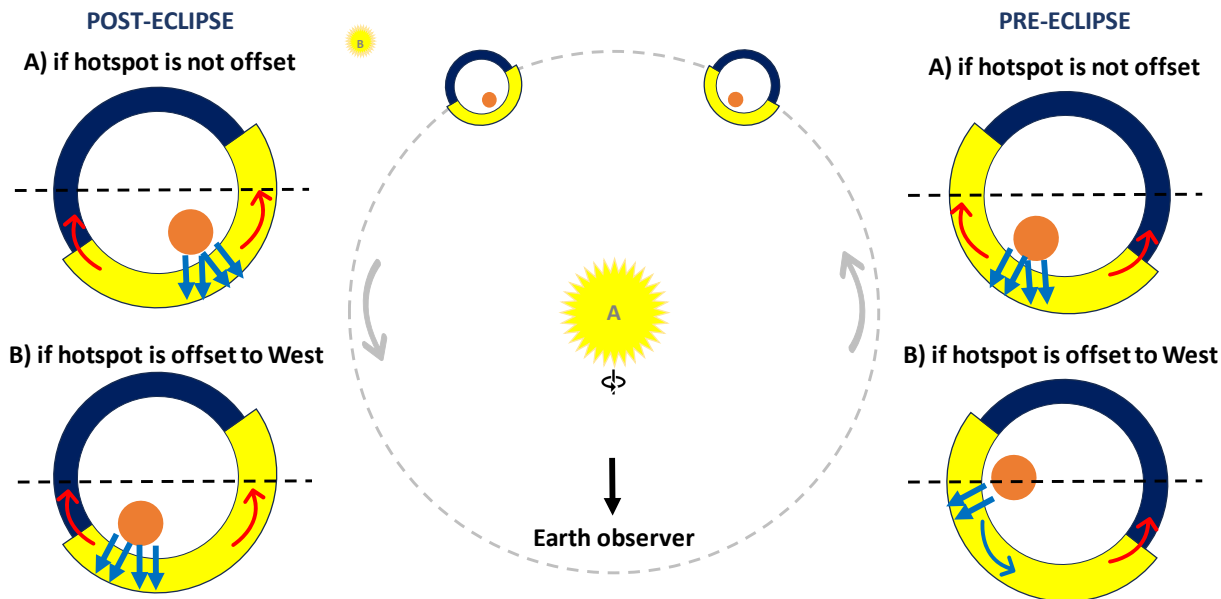


Fig. 8. Geometry of the WASP-76 b system. The planet is shown from a polar perspective, at different phases of its orbit, with the inflated dayside in yellow and the nightside in dark blue. The orange circle is the hotspot, for which we consider two possible locations: (A) at the substellar point (no offset) or (B) with a westward offset; to compare the possible atmospheric dynamics of each case. The arrows represent the motion of winds, and whether they appear blueshifted or redshifted to an observer on Earth. The dashed black line separates the hemisphere visible to the observer from the non-visible one. A proposed scenario of atmospheric circulation that could lead to the results of this work is presented in the text (see Sect. 5.1 for discussion).

the observational data with synthetic models of these chemical species computed with `petitRADTRANS`. Furthermore, detecting emission features confirms the existence of an inverted atmospheric profile. We then investigated how the pressure-temperature profile impacted the emission signature, by computing synthetic templates based on varying P-T profiles and comparing the resulting CCFs. Our results are summarised as follows:

1. We detect a blueshifted signature (-4.7 ± 0.3 km/s) of Fe I in nearly all epochs, with a detection significance of 6.0σ from the co-added CCF of the four epochs.
2. We confirm the existence of a thermal inversion layer, which follows from the fact that emission features can only be present if the dayside has an inverted structure.
3. We report a non-detection of Fe II. Due to the hot temperature of this planet, we expect this ion to exist in the outer atmosphere. However, the non-detection could be due Fe II being more abundant in the outer atmosphere, which is optically thinner and thus harder to probe with emission spectroscopy. Follow-up studies are required to confirm its presence.
4. We discuss possible atmospheric scenarios to explain the blueshifted signature. We propose that material is being radially ejected from the hotspot, rising in the atmosphere, and proceeding to the cooler nightside of the planet. We strongly encourage the development of GCM studies that could reproduce this feature.
5. Based on the change of RV shift measured in individual epochs, we are unable to constrain whether the hotspot is located at the substellar point or if it is offset. Further observations are required to disentangle the two scenarios.
6. The Fe I signal strength changes when we compare the CCFs resulting from different assumptions of P-T profile. The

strongest significance is attributed to a profile where the temperature of the upper atmosphere is 3500 K and the lower atmosphere is 1200 K, with the inversion located between 1–100 mbar.

In recent years, emission spectroscopy has often been seen as ill-favoured compared to transmission spectroscopy due to the glaring difference in signal strength. However, it is the best spectroscopic avenue to probe the atmospheric structure and composition of exoplanets' dayside, thus being a crucial technique for exoplanet research. In the lead-up to the next generation of ground-based spectrographs, such as ANDES at the Extremely Large Telescope (Marconi et al. 2022), we provide an example of how useful ground-based high-resolution instruments are for characterising exoplanets. We highlight, in particular, the capability of ESPRESSO to probe the dayside of ultra hot Jupiters, in order to constrain their chemical composition and probe the dynamics of atmospheric circulation.

Acknowledgements. We thank the anonymous referee for their comments which helped improve the manuscript. The authors acknowledge the ESPRESSO project team for its effort and dedication in building the ESPRESSO instrument. This work was supported by the Fundação para a Ciência e Tecnologia (FCT) and POCH/FSE through the research grants UIDB/04434/2020 and UIDP/04434/2020, and in the framework of the project 2022.04048.PTDC (Phi in the Sky, DOI 10.54499/2022.04048.PTDC). This work was co-funded by the European Union (ERC, FIERCE, 101052347). This project has received funding from the European Research Council (ERC) under the European Union's Horizon 2020 research and innovation programme (project SPICE DUNE, grant agreement No 947634). Views and opinions expressed are however those of the authors only and do not necessarily reflect those of the European Union or the European Research Council. Neither the European Union nor the granting authority can be held responsible for them. The authors acknowledge the financial support of the Swiss National Science Foundation (SNSF). This work has also been carried out within the framework of the National Centre of Competence in Research (NCCR) PlanetS supported by the SNSF un-

der the grants 51NF40_182901 and 51NF40_205606. A.R.C.S. acknowledges support from FCT through the fellowship 2021.07856.BD. O.D.S.D. is supported in the form of a work contract (DL 57/2016/CP1364/CT0004) funded by national funds through FCT. C.L. and F.P. would like to acknowledge the SNSF for supporting research with ESPRESSO through the SNSF grants nr. 140649, 152721, 166227, 184618 and 215190. The ESPRESSO Instrument Project was partially funded through SNSF's FLARE Programme for large infrastructures. H.C. and M.L. acknowledge the support of the SNCF under grant number PCEFP2_194576. M.R.Z.O. and E.H.-C. acknowledge financial support from the Agencia Estatal de Investigación (AEI/10.13039/501100011033) of the Ministerio de Ciencia e Innovación and the ERDF "A way of making Europe" through project PID2022-137241NB-C42. E.H.-C. acknowledges support from grant PRE2020-094770 under project PID2019-109522GB-C51 funded by the Spanish Ministry of Science and Innovation/State Agency of Research, MCIN/AEI/10.13039/501100011033, and by ERDF, "A way of making Europe". A.S.M. acknowledges financial support from the Government of the Canary Islands project ProID2020010129. A.S.M., J.I.G.H., and R.R. acknowledge financial support from the Spanish Ministry of Science and Innovation (MICINN) project PID2020-117493GB-I00. S.G.S. acknowledges the support from FCT through Investigador FCT contract nr. CEECIND/00826/2018 and POPH/FSE (EC) (DOI: 10.54499/CEECIND/00826/2018/CP1548/CT0002). S.C. acknowledges financial support from the Italian Ministry of Education, University, and Research with PRIN 201278X4FL and the "Progetti Premiali" funding scheme. C.J.A.P.M. acknowledges FCT and POCH/FSE (EC) support through Investigador FCT Contract 2021.01214.CEECIND/CP1658/CT0001. R.A. is a Trotter Postdoctoral Fellow and acknowledges support from the Trotter Family Foundation. This work was supported in part through a grant from the Fonds de Recherche du Québec - Nature et Technologies (FRQNT). This work was funded by the Institut Trotter de Recherche sur les Exoplanètes (iREX). T.A.S. acknowledges support from FCT through the fellowship PD/BD/150416/2019. E.P. acknowledges financial support from the Agencia Estatal de Investigación of the Ministerio de Ciencia e Innovación MCIN/AEI/10.13039/501100011033 and the ERDF "A way of making Europe" through project PID2021-125627OB-C32, and from the Centre of Excellence "Severo Ochoa" award to the Instituto de Astrofísica de Canarias. A.M.S. acknowledges support from FCT through the fellowship 2020.05387.BD. M.S. acknowledges financial support from the SNSF for project 200021_200726. E.E.-B. acknowledges financial support from the European Union and the State Agency of Investigation of the Spanish Ministry of Science and Innovation (MICINN) under the grant PRE2020-093107 of the Pre-Doc Program for the Training of Doctors (FPI-SO) through FSE funds.

References

- Alei, E., Konrad, B. S., Angerhausen, D., et al. 2022, *A&A*, 665, A106
- Allart, R., Bourrier, V., Lovis, C., et al. 2018, *Science*, 362, 1384
- Allart, R., Lemée-Jolicoeur, P. B., Jaziri, A. Y., et al. 2023, *A&A*, 677, A164
- Allart, R., Lovis, C., Pino, L., et al. 2017, *A&A*, 606, A144
- Azevedo Silva, T., Demangeon, O. D. S., Santos, N. C., et al. 2022, *A&A*, 666, L10
- Bello-Arufe, A., Cabot, S. H. C., Mendonça, J. M., Buchhave, L. A., & Rathcke, A. D. 2022, *AJ*, 163, 96
- Beltz, H., Rauscher, E., Kempton, E. M. R., et al. 2022a, *AJ*, 164, 140
- Beltz, H., Rauscher, E., Kempton, E. M. R., Malsky, I., & Savel, A. B. 2023, *AJ*, 165, 257
- Beltz, H., Rauscher, E., Roman, M. T., & Guilliat, A. 2022b, *AJ*, 163, 35
- Birkby, J., de Kok, R., Brogi, M., et al. 2013, *The Messenger*, 154, 57
- Bohn, A. J., Southworth, J., Ginski, C., et al. 2020, *A&A*, 635, A73
- Borsa, F., Allart, R., Casasayas-Barris, N., et al. 2021, *A&A*, 645, A24
- Borsa, F., Giacobbe, P., Bonomo, A. S., et al. 2022, *A&A*, 663, A141
- Borsato, N. W., Hoeijmakers, H. J., Prinoth, B., et al. 2023, *A&A*, 673, A158
- Bourrier, V., Ehrenreich, D., Lendl, M., et al. 2020, *A&A*, 635, A205
- Brogi, M. & Line, M. R. 2019, *AJ*, 157, 114
- Brogi, M., Snellen, I. A. G., de Kok, R. J., et al. 2012, *Nature*, 486, 502
- Casasayas-Barris, N., Orell-Miquel, J., Stangret, M., et al. 2021, *A&A*, 654, A163
- Changeat, Q., Edwards, B., Al-Refaie, A. F., et al. 2022, *ApJS*, 260, 3
- Cont, D., Yan, F., Reiners, A., et al. 2022, *A&A*, 668, A53
- Cretignier, M., Francfort, J., Dumusque, X., Allart, R., & Pepe, F. 2020, *A&A*, 640, A42
- Deibert, E. K., de Mooij, E. J. W., Jayawardhana, R., et al. 2021, *ApJ*, 919, L15
- Deibert, E. K., de Mooij, E. J. W., Jayawardhana, R., et al. 2023, *AJ*, 166, 141
- Demangeon, O. D. S., Cubillos, P. E., Singh, V., et al. 2024, *A&A*, 684, A27
- Dorn, R. J., Bristow, P., Smoker, J. V., et al. 2023, *A&A*, 671, A24
- Edwards, B., Changeat, Q., Baeyens, R., et al. 2020, *AJ*, 160, 8
- Ehrenreich, D., Lovis, C., Allart, R., et al. 2020, *Nature*, 580, 597
- Evans, T. M., Sing, D. K., Kataria, T., et al. 2017, *Nature*, 548, 58
- Fisher, C. & Heng, K. 2018, *MNRAS*, 481, 4698
- Fortney, J. J., Lodders, K., Marley, M. S., & Freedman, R. S. 2008, *ApJ*, 678, 1419
- Fu, G., Deming, D., Lothringer, J., et al. 2021, *AJ*, 162, 108
- Gaia Collaboration. 2020, *VizieR Online Data Catalog*, I/350
- Gandhi, S., Kesseli, A., Snellen, I., et al. 2022, *MNRAS*, 515, 749
- Garhart, E., Deming, D., Mandell, A., et al. 2020, *AJ*, 159, 137
- Ginski, C., Mugrauer, M., Seeliger, M., et al. 2016, *MNRAS*, 457, 2173
- Hoeijmakers, H. J., de Kok, R. J., Snellen, I. A. G., et al. 2015, *A&A*, 575, A20
- Hoeijmakers, H. J., Ehrenreich, D., Heng, K., et al. 2018, *Nature*, 560, 453
- Hoeijmakers, H. J., Ehrenreich, D., Kitzmann, D., et al. 2019, *A&A*, 627, A165
- Hoeijmakers, H. J., Kitzmann, D., Morris, B. M., et al. 2024, *A&A*, 685, A139
- Høg, E., Fabricius, C., Makarov, V. V., et al. 2000, *A&A*, 355, L27
- Hubeny, I., Burrows, A., & Sudarsky, D. 2003, *ApJ*, 594, 1011
- Kasper, D., Bean, J. L., Line, M. R., et al. 2023, *AJ*, 165, 7
- Kausch, W., Noll, S., Smette, A., et al. 2015, *A&A*, 576, A78
- Kawauchi, K., Narita, N., Sato, B., & Kawashima, Y. 2022, *PASJ*, 74, 225
- Kesseli, A. Y. & Snellen, I. A. G. 2021, *ApJ*, 908, L17
- Kesseli, A. Y., Snellen, I. A. G., Casasayas-Barris, N., Mollière, P., & Sánchez-López, A. 2022, *AJ*, 163, 107
- Lampón, M., López-Puertas, M., Sanz-Forcada, J., et al. 2023, *A&A*, 673, A140
- Landman, R., Sánchez-López, A., Mollière, P., et al. 2021, *A&A*, 656, A119
- Lang, D., Hogg, D. W., Mierle, K., Blanton, M., & Roweis, S. 2010, *AJ*, 139, 1782
- Lendl, M., Anderson, D. R., Collier-Cameron, A., et al. 2012, *A&A*, 544, A72
- Line, M. R., Brogi, M., Bean, J. L., et al. 2021, *Nature*, 598, 580
- Lodders, K. 2020, *Solar Elemental Abundances* (Oxford University Press), arXiv:1912.00844
- Lothringer, J. D. & Barman, T. 2019, *ApJ*, 876, 69
- Lothringer, J. D., Barman, T., & Koskinen, T. 2018, *ApJ*, 866, 27
- Madhusudhan, N. 2019, *ARA&A*, 57, 617
- Marconi, A., Abreu, M., Adibekyan, V., et al. 2022, in *Society of Photo-Optical Instrumentation Engineers (SPIE) Conference Series*, Vol. 12184, *Ground-based and Airborne Instrumentation for Astronomy IX*, ed. C. J. Evans, J. J. Bryant, & K. Motohara, 1218424
- May, E. M., Komacek, T. D., Stevenson, K. B., et al. 2021, *AJ*, 162, 158
- Meadows, V. S., Reinhard, C. T., Arney, G. N., et al. 2018, *Astrobiology*, 18, 630
- Mollière, P., Stolker, T., Lacour, S., et al. 2020, *A&A*, 640, A131
- Mollière, P., Wardenier, J. P., van Boekel, R., et al. 2019, *A&A*, 627, A67
- Ngo, H., Knutson, H. A., Hinkley, S., et al. 2016, *ApJ*, 827, 8
- Pelletier, S., Benneke, B., Ali-Dib, M., et al. 2023, *Nature*, 619, 491
- Pelletier, S., Benneke, B., Darveau-Bernier, A., et al. 2021, *The Astronomical Journal*, 162, 73
- Pepe, F., Cristiani, S., Rebolo, R., et al. 2021, *A&A*, 645, A96
- Perna, R., Menou, K., & Rauscher, E. 2010, *ApJ*, 719, 1421
- Petz, S., Johnson, M. C., Asnodkar, A. P., et al. 2024, *MNRAS*, 527, 7079
- Pino, L., Désert, J.-M., Brogi, M., et al. 2020, *ApJ*, 894, L27
- Prinoth, B., Hoeijmakers, H. J., Kitzmann, D., et al. 2022, *Nature Astronomy*, 6, 449
- Prinoth, B., Hoeijmakers, H. J., Pelletier, S., et al. 2023, *A&A*, 678, A182
- Ridder-Harper, A., de Mooij, E., Jayawardhana, R., et al. 2023, *AJ*, 165, 211
- Sainsbury-Martinez, F., Tremblin, P., Schneider, A. D., et al. 2023, *MNRAS*, 524, 1316
- Sánchez-López, A., Landman, R., Mollière, P., et al. 2022, *A&A*, 661, A78
- Savel, A. B., Kempton, E. M. R., Malik, M., et al. 2022, *ApJ*, 926, 85
- Scandariato, G., Borsa, F., Bonomo, A. S., et al. 2023, *A&A*, 674, A58
- Schneider, A. D., Carone, L., Decin, L., Jørgensen, U. G., & Helling, C. 2022, *A&A*, 666, L11
- Schwieterman, E. W., Kiang, N. Y., Parenteau, M. N., et al. 2018, *Astrobiology*, 18, 663
- Seidel, J. V., Ehrenreich, D., Allart, R., et al. 2021, *A&A*, 653, A73
- Seidel, J. V., Ehrenreich, D., Pino, L., et al. 2020, *A&A*, 633, A86
- Seidel, J. V., Ehrenreich, D., Wyttenbach, A., et al. 2019, *A&A*, 623, A166
- Silva, A. M., Faria, J. P., Santos, N. C., et al. 2022, *A&A*, 663, A143
- Smette, A., Sana, H., Noll, S., et al. 2015, *A&A*, 576, A77
- Snellen, I. A. G., de Kok, R. J., de Mooij, E. J. W., & Albrecht, S. 2010, *Nature*, 465, 1049
- Soubiran, C., Jasniewicz, G., Chemin, L., et al. 2018, *A&A*, 616, A7
- Tabernero, H. M., Zapatero Osorio, M. R., Allart, R., et al. 2021, *A&A*, 646, A158
- Tsiaras, A., Waldmann, I. P., Zingales, T., et al. 2018, *AJ*, 155, 156
- Valente, E. F. S. & Correia, A. C. M. 2022, *A&A*, 665, A130
- Žák, J., Kabáth, P., Boffin, H. M. J., Ivanov, V. D., & Skarka, M. 2019, *AJ*, 158, 120
- Wardenier, J. P., Parmentier, V., Lee, E. K. H., Line, M. R., & Gharib-Nezhad, E. 2021, *MNRAS*, 506, 1258
- Wardenier, J. P., Parmentier, V., Line, M. R., & Lee, E. K. H. 2023, *MNRAS*, 525, 4942
- West, R. G., HELLIER, C., Almenara, J. M., et al. 2016, *A&A*, 585, A126
- Wöllert, M. & Brandner, W. 2015, *A&A*, 579, A129
- Wyttenbach, A., Ehrenreich, D., Lovis, C., Udry, S., & Pepe, F. 2015, *A&A*, 577, A62
- Yan, F., Nortmann, L., Reiners, A., et al. 2023, *A&A*, 672, A107
- Yan, F., Pallé, E., Reiners, A., et al. 2020, *A&A*, 640, L5
- Yan, F., Reiners, A., Pallé, E., et al. 2022, *A&A*, 659, A7

Appendix A: $K_p - v_{\text{sys}}$ plots.

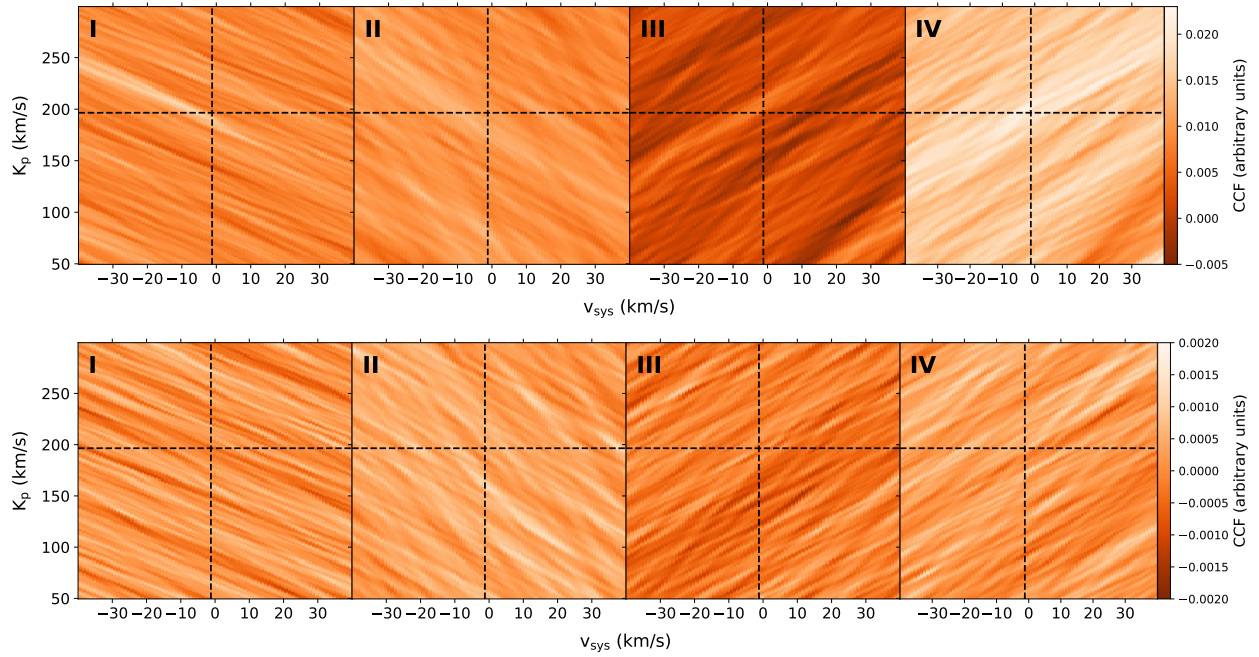


Fig. A.1. $K_p - v_{\text{sys}}$ plots of Fe I and Fe II for each epoch. The dashed black lines mark the expected position of the planetary signal. **Top:** Fe I. The signal is detected in all epochs, though at different amplitudes. **Bottom:** Fe II. No detections are found (see Sect. 5.2 for discussion).

Appendix B: P-T profile exploration

Table B.1. Details of the P-T profiles used to create templates in `peti tRADTRANS`.

P-T #	T_{lower} (K)	T_{upper} (K)	P_{lower} (bar)	P_{upper} (bar)
1	1700	3500	0.106136	0.001095
2	1700	3500	5.546040	0.057201
3	1700	3500	0.011466	0.000118
4	2200	3500	0.106136	0.001095
5	1700	3500	0.467905	0.004826
6	1700	3000	0.106136	0.001095
7	1700	4000	0.106136	0.001095
8	1200	3500	0.106136	0.001095
9	1700	4500	0.106136	0.001095
10	1700	5000	0.106136	0.001095

Notes. Pressure (P) and temperature (T) values are given for the lower and upper boundaries of the thermal inversion layer.

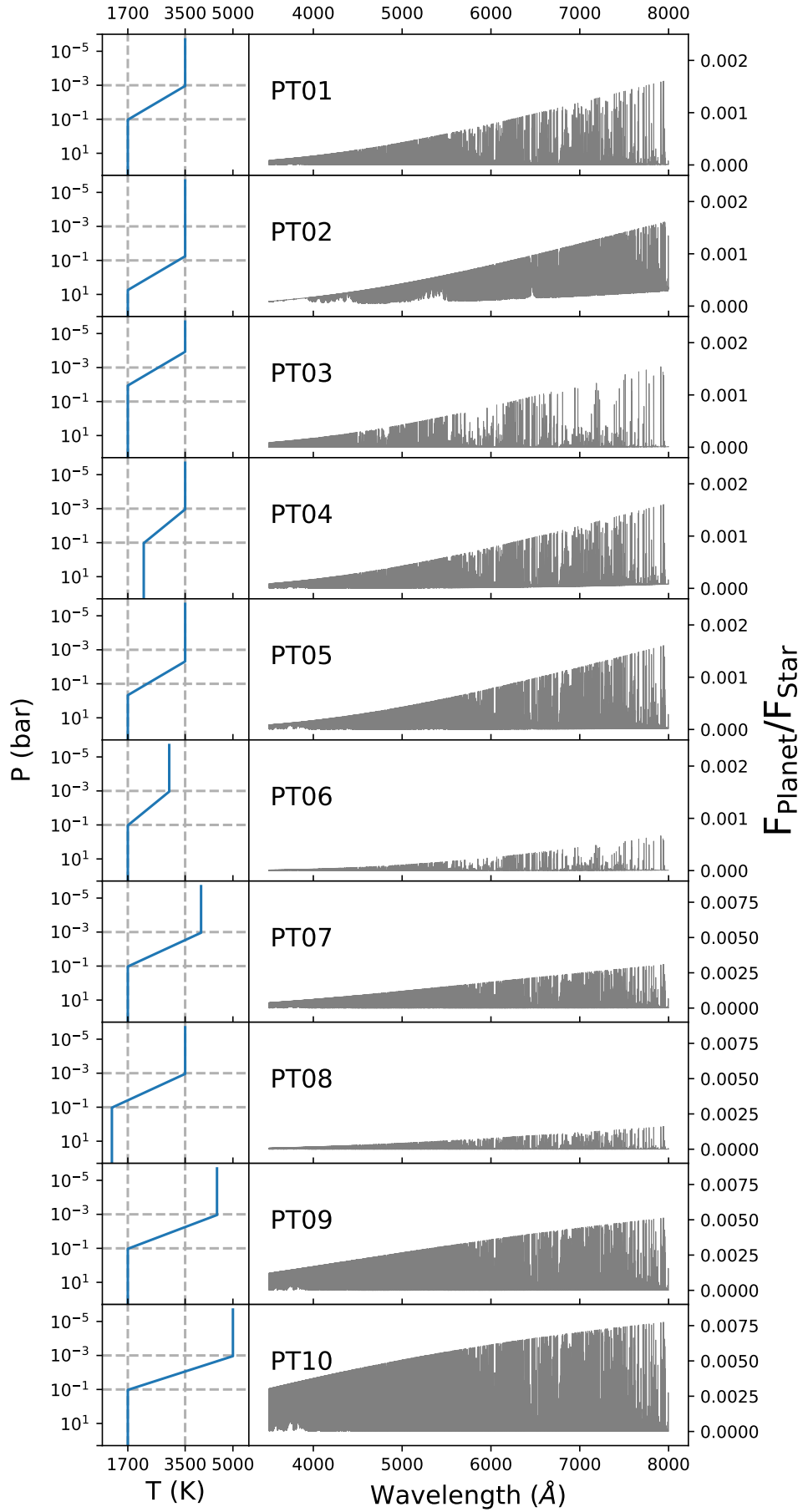


Fig. B.1. petitRADTRANS templates (right) corresponding to the P-T profiles (left), which were utilised for computing the Fe I CCFs. We note that the bottom four models are presented on a larger y-scale than the first six. See Table B.1 for more details on the atmospheric profiles.